



# Nanostructured ceria-based catalysts for soot combustion: Investigations on the surface sensitivity



Marco Piumetti, Samir Bensaid, Nunzio Russo, Debora Fino\*

Department of Applied Science and Technology, Politecnico di Torino, Corso Duca degli Abruzzi 24, 10129 Turin, Italy

## ARTICLE INFO

### Article history:

Received 24 July 2014

Received in revised form 17 October 2014

Accepted 22 October 2014

Available online 31 October 2014

### Keywords:

Ceria

Soot oxidation

Nanostructured materials

Nanocubes

Surface sensitivity

## ABSTRACT

A set of ceria nanomaterials with different topological and textural properties has been prepared to investigate the shape-dependency activity of ceria towards soot combustion under different reaction conditions (namely in “loose” and “tight” contact). The physico-chemical properties of the prepared catalysts have been studied using complementary techniques. The best performances, in terms of the total oxidation of soot, have been achieved for the  $\text{CeO}_2$ -nanocubes, due to the abundance of coordinative unsaturated atomic sites on the (100) and (110) exposed surfaces (namely truncated nanocubes). However, better results, in terms of the onset of soot oxidation, have been obtained for high-surface-area materials, thus reflecting the key role of surface area at low temperatures. Activity tests have suggested the surface-sensitivity of soot oxidation over the prepared ceria-based materials, when the reaction temperature was above  $410^\circ\text{C}$  or  $370^\circ\text{C}$  (in “loose” or “tight” conditions, respectively). On the other hand, the reaction has appeared surface-insensitive at a lower temperature. Hence, soot oxidation over these ceria compounds can be considered a reaction that displays both surface-sensitive and surface-insensitive behaviour, which depend on the experimental conditions.

© 2014 Elsevier B.V. All rights reserved.

## 1. Introduction

Diesel and gasoline engines are sources of the main outdoor air pollutants, such as volatile organic compounds (VOCs),  $\text{NO}_x$  and particulate matter (PM), whose reduction represents a very challenging task [1–3]. Diesel particulate emissions are suspected of causing several health problems, including lung cancer, and hence research into soot abatement in the exhaust of diesel engines has received much interest over the last few years [4–7]. Recent legislation has introduced more stringent  $\text{NO}_x$  and particulate limits for light and heavy-duty vehicles as well as for passenger cars, and has imposed the use of catalytic devices to satisfy the required standards [1,3,7].

The solid carbon (soot) that forms diesel exhaust particulates can be burnt off above  $600^\circ\text{C}$ , although typical diesel engine exhaust temperatures fall within the  $200$ – $500^\circ\text{C}$  range [7,8]. Therefore, oxidation catalysts can be used to increase the oxidation rate of filter traps at lower temperatures. Ceria-based materials are among the most active soot oxidation catalysts under either  $\text{O}_2$  or in a  $\text{NO}_x/\text{O}_2$  atmosphere. Ceria alone, or in combination with other metal oxides, may exhibit promising soot oxidation

activity [1,4,9–14]. The redox behaviour, as well as the availability of chemisorbed oxygens ( $\alpha$ -species), are the most important factors that play a role on the oxidation activity of  $\text{CeO}_2$ -based materials [15–19]. However, the number of soot-catalyst contact points also affects the catalytic activity of ceria for soot oxidation and it is therefore necessary to maximize the interaction between the soot particles and the catalyst surface [10,13].

Over the last few decades, there has been significant progress in the nanoscale controlled synthesis of  $\text{CeO}_2$ -based materials for a number of catalytic applications. Different shapes and sizes of ceria have been synthesized using methods designed by many research groups [20]. In general, nanostructured materials are notable because of their small featured size, which endows them with size- and shape-dependent properties due to the high surface-to-volume ratio (=higher number of coordinatively unsaturated sites), and their unique electronic features (quantum size effects) [21–26]. Hence, the catalytic activity of nanomaterials depends not only on the crystal size, but also on the crystal surfaces and thus on the exposed planes [27–29]. The higher chemical reactivity of specific ceria surfaces has been confirmed in a number of reactions, such as CO oxidation,  $\text{CO}_2$  reforming of methane, methanol and ethanol reforming and low-temperature WGS and, more recently, soot oxidation [30–37].

Ceria nanomaterials with well-defined reactive (100) and (110) planes are usually more active than conventional

\* Corresponding author. Tel.: +39 011 0904710; fax: +39 011 0904699.  
E-mail address: [debora.fino@polito.it](mailto:debora.fino@polito.it) (D. Fino).

polycrystalline ceria NPs with preferred exposure of (111) planes [38]. Data reported for several catalytic reactions suggest that the order of chemical reactivity for CeO<sub>2</sub>-nanostructures is nanocubes > nanorods > polycrystalline ceria NPs [38,39]. This sequence reflects the reverse order of the surface stability of ceria: (100) and (110) < (111) facets [38–41]. However, it has been observed, for both CO and soot oxidation, that the thermal treatment of polycrystalline ceria at  $T > 500^\circ\text{C}$  promotes the exposure of more reactive surfaces, such as (100) and (110) facets, whereas it progressively reduces exposure of less reactive surfaces, such as (111) planes [9].

However, the beneficial role of the textural properties (e.g. specific surface area, total pore volume, pore diameter and so on) on the overall catalytic activity of CeO<sub>2</sub> for various reactions, including soot combustion, is well known [1,9]. Therefore, it is necessary to maximize the exposure of more reactive surfaces of CeO<sub>2</sub> using high surface area materials as supports.

In the present work, a set of CeO<sub>2</sub> samples with different topological and textural properties (CeO<sub>2</sub>-nanocubes, CeO<sub>2</sub>-nanorods over ZSM-5-type zeolite, CeO<sub>2</sub>-nanorods, mesoporous CeO<sub>2</sub> and CeO<sub>2</sub>-SCS) has been prepared to investigate the shape-dependency activity of ceria towards soot combustion under different reaction conditions (namely in “loose” and “tight” contact). The physico-chemical properties of the prepared catalysts were studied using complementary techniques.

## 2. Experimental

### 2.1. Preparation of the samples

CeO<sub>2</sub>-nanorods and CeO<sub>2</sub>-nanocubes (denoted hereafter as Ce-NR and Ce-NC, respectively) have been synthesized through the hydrothermal procedure [42,43]. During a typical synthesis, appropriate amounts of NaOH (24 g) and Ce(NO<sub>3</sub>)<sub>3</sub>·6H<sub>2</sub>O (2.2 g) (Sigma-Aldrich) were dissolved in 35 mL and 5 mL of bi-distilled water, respectively. The two solutions were then mixed together and stirred for 1 h, which resulted in the formation of a milky slurry. The final mixture was transferred to an autoclave (150 mL) which was 75% filled with deionised water. The mixture was then aged at either 100 °C (to form nanorods) or at 165 °C (to form nanocubes) for 24 h. The fresh precipitates were then separated by centrifugation, washed with deionised water several times, washed in ethanol and dried at 60 °C overnight. The powders were calcined at 550 °C in synthetic air for 4 h.

The synthesis of the mesoporous ceria (denoted as Ce-M) was [42]: 2.5 g of Ce(NO<sub>3</sub>)<sub>3</sub>·6H<sub>2</sub>O (Sigma-Aldrich) was dissolved in 20 mL of absolute ethanol. 0.5 g SBA-15 (ACS materials) was added to this solution and heated at 60 °C under vigorous stirring. After the ethanol had evaporated, the cerium precursor/silica composite was calcined at 450 °C for 4 h. The procedure was repeated once more with an ethanol solution of 1.2 g Ce(NO<sub>3</sub>)<sub>3</sub>·6H<sub>2</sub>O. The powder was dried at 110 °C overnight and calcined at 550 °C in synthetic air for 4 h. The silica template was then removed and treated three times with 2 M NaOH solution at 50 °C (10 min each time). Finally, the obtained product was dried at 60 °C overnight.

The Ce-NC/ZSM-5 sample was prepared by adding an appropriate amount of Ce-NC solution to the ZSM-5 type zeolite (Zeolyst International) and placing the mixture in a rotary evaporator at 60 °C in order to progressively evacuate the water. The obtained solid (CeO<sub>2</sub>/ZSM-5 = 1.0 by weight) was then dried at 90 °C overnight.

A comparative mesoporous sample (denoted as Ce-SCS) was prepared by solution combustion synthesis (SCS) [2,45]. In short, a homogeneous aqueous solution of Ce(NO<sub>3</sub>)<sub>3</sub>·6H<sub>2</sub>O (1.9 g) (Sigma-Aldrich) and urea (0.8 g), prepared at room temperature,

was placed in an oven at 600 °C for 20 min. The resultant powder was washed with deionised water to remove impurities and then dried overnight.

### 2.2. Characterization of the catalysts

The powder X-ray diffraction patterns have been collected on a X'Pert Philips PW3040 diffractometer using Cu K $\alpha$  radiation ( $2\theta$  range = 20–70°; step = 0.05°  $2\theta$ ; time per step = 0.2 s). The diffraction peaks were indexed according to the Powder Data File database (PDF 2000, International Centre of Diffraction Data, Pennsylvania). The average size of the crystallites was determined using the Scherrer formula,  $D = 0.9\lambda/b \cos \theta$ , where  $\lambda$  is the wavelength of the Cu K $\alpha$  radiation,  $b$  is the full width at half maximum (in radians), 0.9 is the shape factor for spherical particles and  $\theta$  is the angle of the diffraction peaks.

Specific surface area ( $S_{\text{BET}}$ ), total pore volume ( $V_p$ ) and average pore diameter ( $D_p$ ) were measured by means of N<sub>2</sub> physisorption at –196 °C (Micrometrics ASAP 2020) on samples previously outgassed at 200 °C for 4 h to remove water and other atmospheric contaminants. The specific surface area of the samples was calculated using the BET method, and the pore diameters were evaluated by applying the Barrett-Joyner-Halenda (BJH) algorithm to the isotherm desorption branch.

Sample morphology was investigated by means of a field emission scanning electron microscope (FESEM Zeiss MERLIN, Gemini-II column) and transmission electron microscopy (TEM, Jeol JEM 3010 operating at 200 kV). The Si-content in the Ce-M sample was determined through EDS analysis (Oxford X-ACT): three different spots with a 10–50 nm diameter were selected in representative zones of the sample, and the average Si-content was then calculated.

For H<sub>2</sub>-TPR measurements, 50 mg catalyst was pre-treated under air flow (40 cm<sup>3</sup> min<sup>–1</sup>) at 150 °C for 1 h, to remove water and other atmospheric contaminants, and subsequently cooled to 25 °C with Ar. TPR analysis was carried out by heating the sample up to 950 °C at a constant rate of 5 °C min<sup>–1</sup> under an Ar flow (4.95% molar H<sub>2</sub> in Ar). H<sub>2</sub> consumption was recorded using a thermal conductivity detector (TCD).

XPS (X-ray photoelectron spectroscopy) measurements were obtained on XPS PHI 5000 Versa probe apparatus using a band-pass energy of 187.85 eV, a 45° take off angle and a 100.0  $\mu\text{m}$  diameter X-ray spot size. Curve-fits were performed by means of Multipack 9.0 software.

### 2.3. Catalytic activity tests

The soot oxidation activity of the catalysts has been measured by means of temperature programmed oxidation (TPO), which was carried out in a fixed-bed micro-reactor (a quartz U-tube, with an inner diameter of 4 mm, heated by an electric furnace). The temperature was measured by a thermocouple placed close to the middle of the catalytic bed. An N<sub>2</sub> flow, containing 10% of O<sub>2</sub>, was fed at a constant rate of 100 cm<sup>3</sup> min<sup>–1</sup>, to the fixed bed, which was constituted by 50 mg of a carbon mixture (Printex-U) and powdered catalyst (=45 mg of catalyst and 5 mg of soot) mixed with 150 mg of inert silica. Two types of contact conditions were considered:

- “Loose” contact: the catalyst–soot mixture was prepared by gently shaking it with a spatula in a polyethylene vessel for 1 min. This procedure was sufficient to homogenize the mixture, but still allowed the two solid phases to be loosely put in contact. Although the procedure was very short, the established contact led to a reproducible catalytic performance;
- “Tight” contact: the catalyst–soot mixture was obtained through a 10 min ball milling at 250 rpm (IG/W2/E, Giuliani Tecnologie) to reach a close contact between the catalyst and soot. This

method maximizes the number of contact points and, although it is less representative of the real contact conditions that occur in a catalytic trap for diesel particulate removal, it is better able to discriminate the different morphologies [46].

The reaction temperature was controlled by means of a PID-regulated oven and varied from 200 to 700 °C at a 5 °C min<sup>-1</sup> rate. The CO/CO<sub>2</sub> concentration in the outlet gas was measured via NDIR analyzers (ABB). Each test was repeated three times to ensure the reproducibility of the obtained results: the maximum deviation from the mean value over the three tests was  $\pm 5$  °C (ca. 1% of the measured temperature). Temperatures corresponding to 10%, 50%, 90% and 100% soot conversion (denoted as  $T_{10}$ ,  $T_{50}$ ,  $T_{90}$  and  $T_{peak}$ , respectively) were taken as indices of the activity of the tested catalysts.

### 3. Result and discussion

#### 3.1. Textural properties of the materials

Table 1 shows the main textural properties of all the samples, derived from both the powder XRD patterns and N<sub>2</sub> physisorption isotherms.

Fig. 1 reports the XRD spectra of the CeO<sub>2</sub>-based materials: the patterns are very similar and the main peaks can be indexed to (111), (200), (220), (311), (222) and (400) planes, according to a cubic fluorite structure [47,48]. The XRD reflections of the Ce-M sample are relatively broad and low in intensity, since the mesoporous walls of this material are formed by nanocrystalline CeO<sub>2</sub> frameworks [44,48]. The low-angle XRD pattern of this sample (inset in Fig. 1) shows that the replication of the SBA-15 template was only preserved slightly, since the main peak due to  $d_{(100)}$  reflection appears. However,  $d_{(110)}$  and  $d_{(200)}$  reflections are not observed, thus indicating that the nanocasting procedure leads to less ordered materials than the SBA-15 template. When Ce-M is compared with the SBA-15 template (not reported for the sake of brevity), these peaks are broad and low in intensity, again confirming that the Ce-M sample is much less ordered than the silica template, in agreement with previous work [44,49]. Although it is relatively difficult to evaluate the average particle size from Scherrer's formula for nanoshapes that differ from spherical geometry, this estimation was performed to corroborate the TEM analysis results. Application of Scherrer's formula led to the following particle sizes: 54 nm (Ce-NC), 43 nm (Ce-NR) and 5 nm (Ce-M). Comparable sizes were also observed for the Ce-SCS sample, which consisted of particles with a diameter of about 35 nm. These findings are in agreement with previous XRD analysis for CeO<sub>2</sub>-based materials [9,44,49].

The BET surface areas of both the Ce-NC and Ce-NR samples are very low as are the total pore volumes (data in Table 1). As expected, the Ce-NC/ZSM-5 sample exhibits much better textural properties ( $S_{BET} = 425 \text{ m}^2 \text{ g}^{-1}$  and  $V_p = 0.20 \text{ cm}^3 \text{ g}^{-1}$ ) than Ce-NC, due to

**Table 1**  
Textural properties of the samples, as derived by both XRD analysis and N<sub>2</sub> isotherms at -196 °C.

Catalyst	Particle size <sup>a</sup> (nm)	$S_{BET}$ (m <sup>2</sup> g <sup>-1</sup> )	$V_p$ <sup>b</sup> (cm <sup>3</sup> g <sup>-1</sup> )	$D_p$ <sup>c</sup> (nm)
Ce-NC	54	4	0.01	–
Ce-NR	43	4	0.01	–
Ce-NC/ZSM-5	54	425	0.20	0.5
Ce-M	5	75	0.15	4
Ce-SCS	35	69	0.04	2

<sup>a</sup> Calculated applying the Scherrer formula.

<sup>b</sup> Total pore volume.

<sup>c</sup> Pore diameter calculated according to the BJH method.

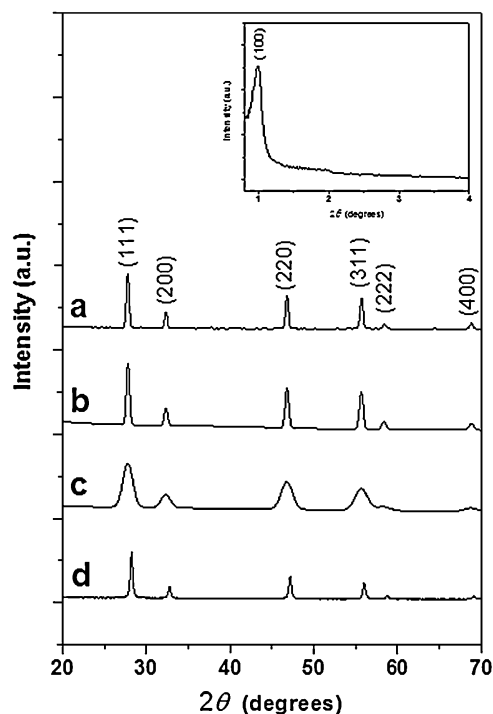


**Fig. 1.** Powder wide-angle XRD patterns of the (a) Ce-NC, (b) Ce-NR, (c) Ce-M and (d) Ce-SCS samples. Inset: low-angle XRD of the Ce-M sample.

the high surface area zeolite which has 3-D channels and cavities of molecular dimensions. Thus, the ZSM-5-type support should be able to promote the oxidation activity of CeO<sub>2</sub> nanocubes, due to the better dispersion of the latter; longer residence times of the molecules on the solid surface should also favour deeper oxidation [50].

The mesostructured Ce-M sample exhibits a BET surface area of 75 m<sup>2</sup> g<sup>-1</sup> and a total pore volume of 0.15 cm<sup>3</sup> g<sup>-1</sup>. These textural values are much lower than those of the employed SBA-15 hard template ( $S_{BET} = 724 \text{ m}^2 \text{ g}^{-1}$  and  $V_p = 0.80 \text{ cm}^3 \text{ g}^{-1}$ ), as already observed in previous studies [44,49]. Fig. 2 shows N<sub>2</sub> isotherms at -196 °C of the Ce-M and Ce-NC/ZSM-5 samples: the former (curve a) exhibits type IV isotherms, which is typical of mesoporous materials (adsorption jump at  $p/p^0 \approx 0.5$ –0.9), whereas the latter (curve

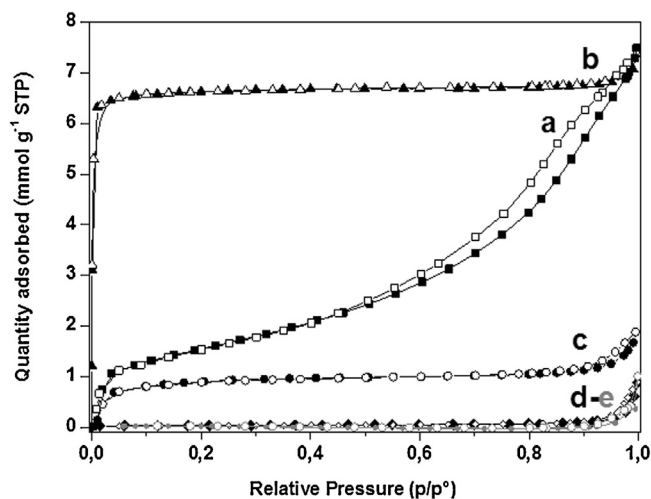


**Fig. 2.** N<sub>2</sub> adsorption/desorption isotherms measured at -196 °C on samples previously outgassed at 200 °C: (a) Ce-M, (b) Ce-NC/ZSM-5, (c) Ce-SCS, (d) Ce-NC and (e) Ce-NR. Full symbols: adsorption branch; white symbols: desorption branch.

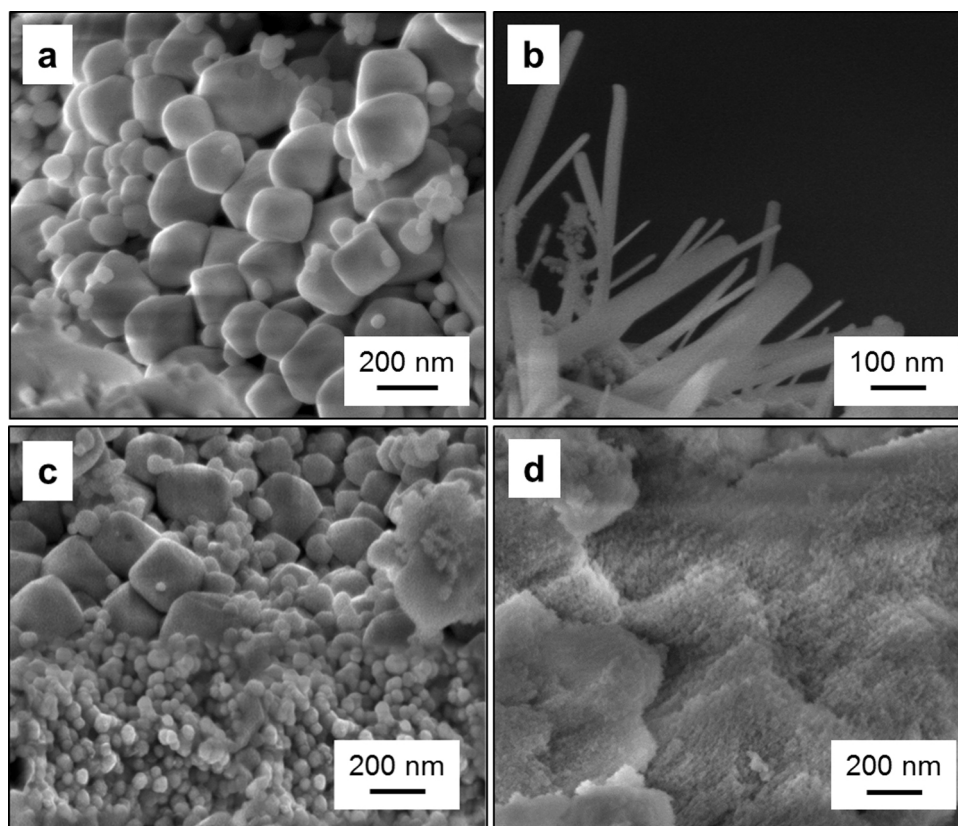


**Fig. 3.** FE-SEM images of the (a) Ce-NC, (b) Ce-NR, (c) Ce-NC/ZSM-5 and (d) Ce-M samples.

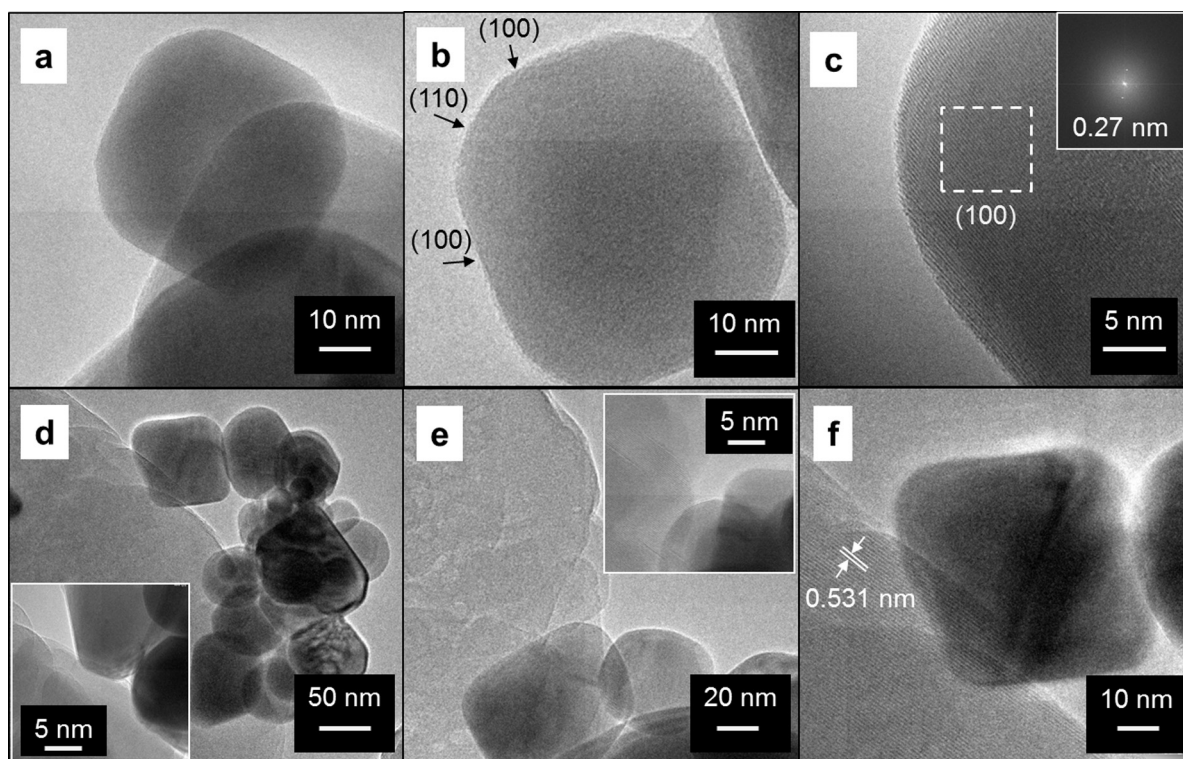


**Fig. 4.** HRTEM images of the (a–c) Ce-NC and (d–f) Ce-NC/ZSM-5 samples.



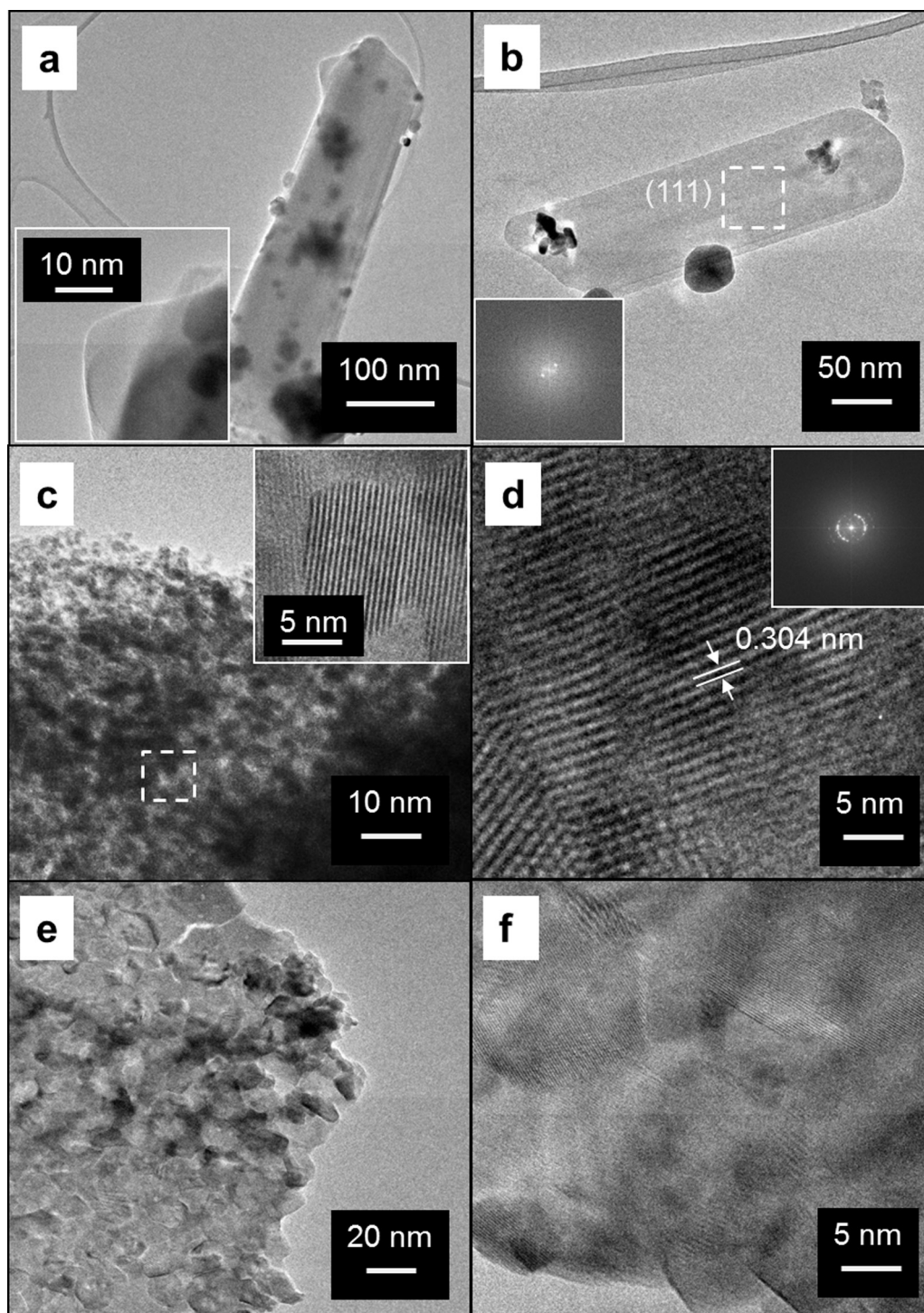


Fig. 5. HRTEM images of the (a and b) Ce-NR, (c and d) Ce-M and (e and f) Ce-SCS samples.

b) is characterized by type I isotherms, with a very steep uptake at low relative pressures (micropore filling), followed by a plateau at near saturation pressure. Comparable  $S_{\text{BET}}$  and  $V_p$  values have been obtained for the Ce-SCS sample (values in Table 1), even though the latter does not present an ordered mesoporous structure, as confirmed by the shape of the adsorption isotherms (curve c). As expected, a much lower adsorption capacity has been achieved for Ce-NC (curve d) and Ce-NR (curve e), due to their particularly low surface areas.

Electron microscopy studies have been carried out to investigate the morphological properties of the prepared samples. The FESEM

images of the Ce-NC and Ce-NR samples, which are reported in Fig. 3a and b, show the characteristic morphologies of nano- $\text{CeO}_2$  (namely cubes and rods, respectively). The sizes of the nanocubes range from 50 to 200 nm, whereas relatively uniform nanorods can be observed, with lengths of about 300–350 nm and an average width of 50 nm. A good dispersion of the  $\text{CeO}_2$ -nanocubes on the surface of ZSM-5 has been obtained for the Ce-NC/ZMS-5 sample, as shown in Fig. 3c. On the other hand, the Ce-M sample (Fig. 3d) presents self-assembled agglomerates of small particles (average size about 50 nm) with interparticle voids, rather than intraparticle porosity. Energy dispersive X-ray analysis (EDS) indicated the

almost complete removal of the silica template from the washed Ce-M sample (not reported for the sake of brevity).

Fig. 4a shows representative TEM images of the CeO<sub>2</sub>-nanocubes in the Ce-NC sample: a careful inspection reveals that the cube corners are actually truncated, and the particles display cuboctahedral structures with an average size of about 50 nm. The micrograph reported in Fig. 4b shows a CeO<sub>2</sub>-nanocube oriented along the [1 0 0] direction with (1 0 0)-type planes at 90°, as reflected by the Fourier transform image (Fig. 4c). The (1 1 0) planes that originate from the truncation of the cube edges are also seen at 45°. These truncated shapes are a result of the reduced surface energy, and given sufficient energy, they exhibit a well-defined cubic structure, as reported elsewhere [43]. The equilibrium shape of such nanostructures is determined by the Wulff rule [51], according to which the convex envelope of planes (perpendicular to the surface normal) minimizes the surface energy for a given enclosed volume [52]. However, the presence of planes with higher Miller indices in truncated cubes has a beneficial effect on surface reactivity [9].

HRTEM images of the Ce-NC/ZSM-5 sample are reported in Fig. 4d–f. As a whole, the micrographies confirm high dispersion and the incorporation of the CeO<sub>2</sub>-nanocubes on the ZSM-5 surface. Moreover, the overlapping of the CeO<sub>2</sub>-nanocubes gives rise to 3-D self-assembled arrays that are spatially accessible to gas-phase molecules (i.e. gaseous oxygen) which promote the surface diffusion. Moreover, the contact points between the soot particles and the CeO<sub>2</sub>-nanocubes increase, thus favouring the formation of active oxygen species (e.g. O<sub>2</sub><sup>−</sup>) through oxygen adsorption on the reduced surface of the ceria in the vicinity of soot [53]. A higher number of surface defects can be observed for the CeO<sub>2</sub>-nanorods, in agreement with recent work [43,54]. The low-magnification HRTEM images of the Ce-NR sample (Fig. 5a and b) in fact reveal the presence of CeO<sub>2</sub>-nanorods with several surface defects due to the HRTEM treatment, as previously observed in [9]. Nevertheless, the CeO<sub>2</sub>-nanorods display a width of 50 nm and a length of about 350 nm, and they are completely crystalline, as confirmed by FESEM and XRD analyses. Fig. 5b shows the (1 1 1) surface exposed by a CeO<sub>2</sub>-nanorod, which is more stable and hence catalytically less reactive than the (1 0 0) and (1 1 0) surfaces [39,54]. In all the representative micrographies that were analyzed, no well-defined (1 1 0) planes were observed in any of the rods considered; this finding is in agreement with the fact that CeO<sub>2</sub>-nanorods mainly expose (1 1 1) planes, whereas nanocubes are mainly composed of (1 0 0) facets [54]. The HRTEM images of the Ce-M sample are reported in Fig. 5c and d. This sample exhibits large domains of CeO<sub>2</sub>, with a certain ordered framework, and uniform nanoparticles, with sizes ranging from 4 to 10 nm, interconnected to each other, which create a 3-D mesoporous network. Fig. 5d shows that such NPs are highly crystalline and display an interplanar spacing of 0.30 nm, corresponding to the (1 1 1) lattice planes of CeO<sub>2</sub>, in agreement with the XRD analysis (see Table 1). The HRTEM images of the Ce-SCS sample (Fig. 5e and f) confirm the presence of ceria domains formed by non-uniform nanoparticles with a size of 20–40 nm.

### 3.2. Reducibility and redox properties of ceria-based materials

The reducibility of the surface and bulk ceria has been investigated through H<sub>2</sub>-TPR analysis. According to the literature, a hydrogen temperature-programmed reduction can offer important indications on the reducibility and the redox behaviour of CeO<sub>2</sub>-based materials [1,55]. The reduction in CeO<sub>2</sub> also depends on the Ce species that are located in different coordinative environments. Moreover, the presence of Ce<sup>3+</sup> ions may reflect structural defects in which the charge imbalance is neutralized by the formation of oxygen ion (O<sup>2−</sup>) vacancies [56–58].

As a whole, the H<sub>2</sub>-TPR profiles of high surface area CeO<sub>2</sub>-based materials are characterized by a low temperature peak in the

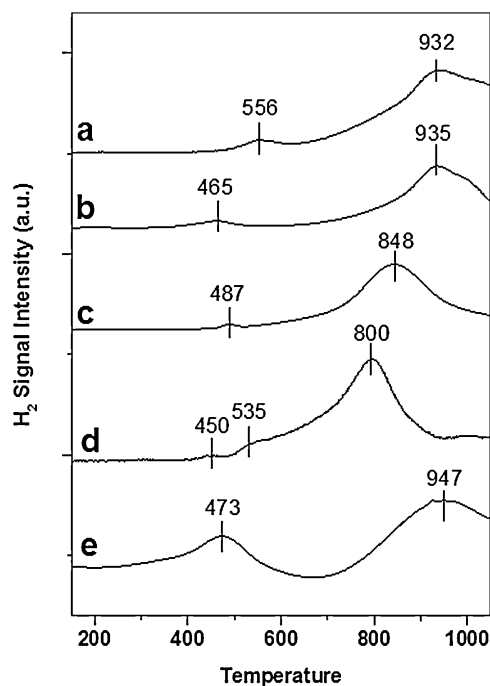


Fig. 6. H<sub>2</sub>-TPR profiles of the (a) Ce-NC, (b) Ce-NR, (c) Ce-NC/ZSM-5, (d) Ce-M and (e) Ce-SCS samples.

300–500 °C range, which is characteristic of surface CeO<sub>2</sub> reduction, and a large peak at higher temperature (700–1000 °C), due to bulk reduction [1,9,55]. The unsaturated surface capping oxygens ( $\alpha$ -species) can easily be removed at a lower temperature than bulk ceria, in which lattice oxygen ions ( $\beta$ -species) have to be transported to the surface before being reduced [59]. On the contrary, the reduction at a low temperature is negligible for low-surface-area materials and only one reduction peak, due to bulk CeO<sub>2</sub>, can usually be observed.

Fig. 6 shows the H<sub>2</sub>-TPR profiles of the fresh samples. The main reduction peaks for both the Ce-NC (curve a) and Ce-NR (curve b) samples appear at 556, 465 °C and 932–936 °C, and correspond to surface and bulk CeO<sub>2</sub> reduction, respectively. Similar results have been obtained with Ce-NC/ZSM-5 (curve c), although a significant decrease in the surface and bulk reduction temperature can be observed for the latter sample, most likely due to the higher amount of chemisorbed oxygens (O<sub>α</sub>). Similarly, the TPR profile of the Ce-M sample (curve d) shows two reduction peaks centred at 450 and 535 °C, due to the surface reduction of small CeO<sub>2</sub> crystals, whereas the bulk reduction only occurs at 800 °C. A quite different TPR profile has been obtained for the Ce-SCS sample (curve e), in which an intense reduction peak appears at 473 °C, most likely due to an easier surface CeO<sub>2</sub> reduction, whereas the bulk reduction appears at about 950 °C.

Fig. 7 reports the XPS spectra in the O 1s and Ce 3d BE regions. The O 1s spectra (Fig. 7A) shows different features, which depend on both the chemisorbed oxygen species (O<sub>α</sub>) and lattice oxygen (O<sub>β</sub>). As a whole, the peak at 529.0–529.7 eV corresponds to O<sub>β</sub> (O<sup>2−</sup>), whereas the signal at 530.8–531.6 eV can be attributed to surface-adsorbed oxygen species (i.e. O<sub>2</sub><sup>2−</sup>, O<sup>−</sup>, OH<sup>−</sup>, CO<sub>3</sub><sup>2−</sup>) [60,44]. The latter signal is more intense with Ce-NC/ZSM-5, Ce-M and Ce-SCS catalysts (curves c, d, e, respectively), as consequence of their high surface areas.

In general, the latter species exhibit higher mobility than lattice oxygen and may give rise to beneficial spillover phenomena at the solid surface [61]. In fact, spillover oxygen can play different roles, in that it may: (i) control the active centres and (ii) serve as a reactant. As reported in Table 2, higher O<sub>α</sub>/O<sub>β</sub> ratios have been

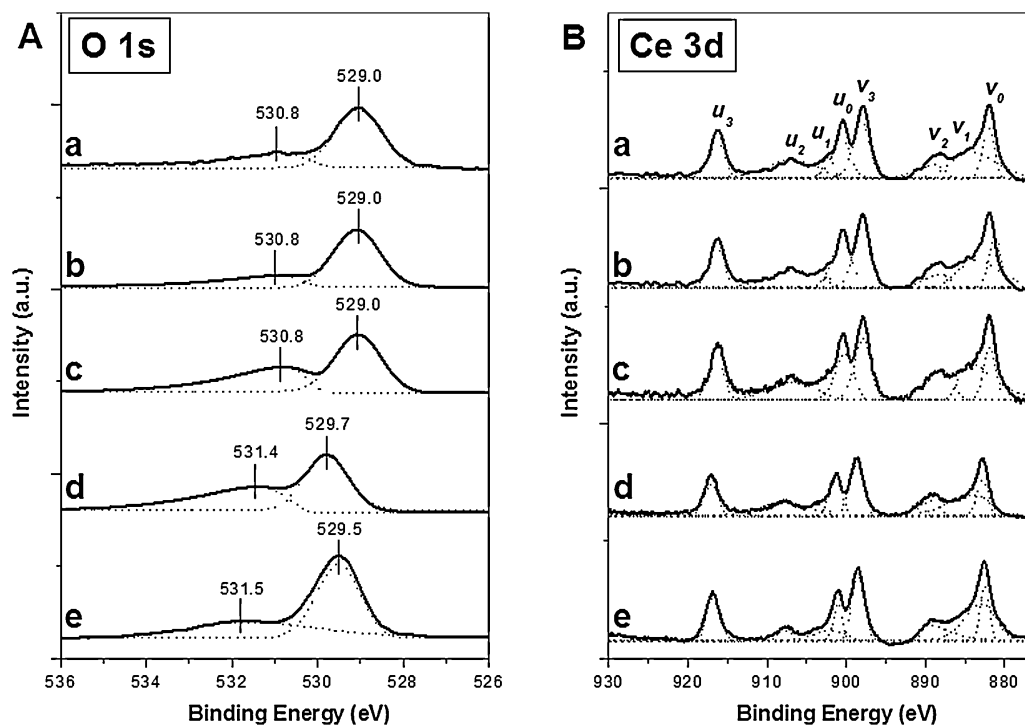


Fig. 7. XPS spectra of the (a) Ce-NC, (b) Ce-NR, (c) Ce-NC/ZSM-5, (d) Ce-M and (e) Ce-SCS samples in the O (1s) (A) and Ce (3d) core level regions (B).

**Table 2**  
Results of curve-fittings on O 1s binding energies of catalysts. The relative ratios of the surface-adsorbed oxygen ( $O_\alpha$ ) and lattice oxygen ( $O_\beta$ ) are reported in the last column.

Sample	$O_\alpha$ (% atom)	$O_\alpha$ BE (eV)	$O_\beta$ (% atom)	$O_\beta$ BE (eV)	$O_\alpha/O_\beta$
Ce-NC	4.1	530.8	95.9	529.0	0.04
Ce-NR	3.6	530.8	96.4	529.0	0.04
Ce-NC/ZSM-5	46.0	530.8	54.0	529.0	0.85
Ce-M	50.9	531.4	49.1	529.7	1.03
Ce-SCS	38.3	531.5	61.7	529.5	0.62

**Table 3A**  
Results of curve-fittings on Ce 3d binding energies of catalysts.

Ce 3d <sub>5/2</sub>							
Sample	$\nu_0$ (Ce <sup>4+</sup> ) (% atom)	$\nu_0$ (Ce <sup>4+</sup> ) BE (eV)	$\nu_1$ (Ce <sup>3+</sup> ) (% atom)	$\nu_1$ (Ce <sup>3+</sup> ) BE (eV)	$\nu_2$ (Ce <sup>4+</sup> ) (% atom)	$\nu_2$ (Ce <sup>4+</sup> ) BE (eV)	$\nu_3$ (Ce <sup>4+</sup> ) (% atom)
Ce-NC	9.5	881.8	24.8	884.1	10.5	888.1	14.7
Ce-NR	9.2	881.8	24.0	884.1	10.1	888.1	17.7
Ce-NC/ZSM-5	11.1	881.8	22.9	884.0	16.1	888.1	18.1
Ce-M	9.6	882.7	24.0	884.0	7.9	889.3	18.0
Ce-SCS	8.1	882.0	27.5	882.9	10.2	889.0	19.8
Ce 3d <sub>3/2</sub>							
Sample	$u_0$ (Ce <sup>4+</sup> ) (% atom)	$u_0$ (Ce <sup>4+</sup> ) BE (eV)	$u_1$ (Ce <sup>3+</sup> ) (% atom)	$u_1$ (Ce <sup>3+</sup> ) BE (eV)	$u_2$ (Ce <sup>4+</sup> ) (% atom)	$u_2$ (Ce <sup>4+</sup> ) BE (eV)	$u_3$ (Ce <sup>4+</sup> ) (% atom)
Ce-NC	13.5	900.5	2.8	902.4	14.1	906.6	10.2
Ce-NR	14.1	900.5	1.5	902.3	13.6	906.6	9.8
Ce-NC/ZSM-5	15.2	900.1	1.9	902.2	3.2	906.6	11.3
Ce-M	12.2	901.2	1.5	902.5	16.3	907.7	10.4
Ce-SCS	7.5	901.0	8.6	902.1	4.4	906.6	13.9

attained for the Ce-M, Ce-NC/ZSM-5 and Ce-SCS samples, thus confirming that higher amounts of surface hydroxyls, carbonates and  $O_2$  appear on the surface of these materials. On the other hand, the Ce-NC and Ce-NR samples mainly present  $O_\beta$  species.

Fig. 7B shows the Ce 3d core-level spectra of the CeO<sub>2</sub>-based samples, where the “ $\nu$ ” and “ $u$ ” peaks correspond to 3d<sub>5/2</sub> and 3d<sub>3/2</sub> states, respectively. The doublets ( $\nu_0, u_0$ ), ( $\nu_2, u_2$ ), and ( $\nu_3, u_3$ ) have

been assigned to the diversified states of Ce<sup>4+</sup>, whereas the doublet ( $\nu_1, u_1$ ) has been attributed to the Ce<sup>3+</sup> species [60]. Therefore, the relative abundance of the Ce<sup>3+</sup> (%) species of each sample has been estimated by considering the deconvolution peaks of Ce 3d binding energies (Tables 3A and 3B).

As a result, the intensity of the doublet ( $\nu_1, u_1$ ) for Ce-SCS is higher than that of the other samples, indicating a larger Ce<sup>3+</sup>



**Table 3B**  
Concentrations of Ce<sup>3+</sup> (%) estimated by XPS signals on Ce 3d binding energies.

Sample	Ce <sup>3+</sup> ( $v_1 + u_1$ ) (%)
Ce-NC	27.6
Ce-NR	25.5
Ce-NC/ZSM-5	24.8
Ce-M	25.5
Ce-SCS	36.1

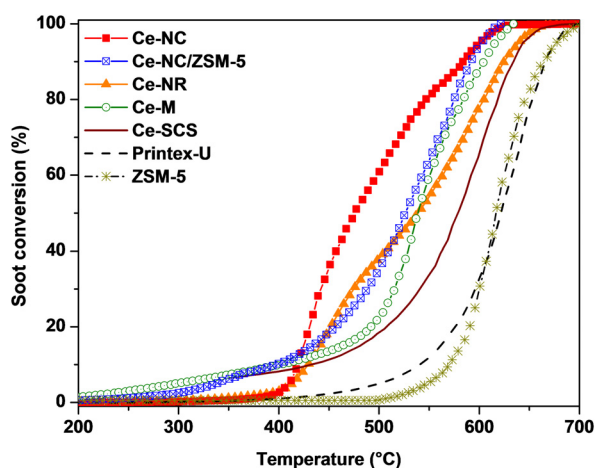


**Fig. 8.** Soot conversion, as a function of temperature, over CeO<sub>2</sub>-based catalysts, pure ZSM-5 and Printex-U (no catalyst) using “loose” contact conditions.

content on the surface (namely 36.1%), which can be attributed to the high temperature used during the combustion synthesis (600 °C) [61]. These findings also confirm the easier reducibility of the Ce-SCS surface, which is mainly due to the presence of the chemisorbed O<sub>α</sub> species that are weakly bonded to the solid catalyst.

### 3.3. Soot oxidation activity

The prepared catalysts were tested for soot combustion in TPO runs in order to study the effect of topological and textural properties on the catalytic activity. Fig. 8 shows the soot conversion to CO<sub>2</sub> as a function of the temperature obtained with the CeO<sub>2</sub>-based catalysts (in loose contact) along with Printex-U (no catalyst). The ZSM-5-type support has also been tested and showed comparable conversion values with those achieved with Printex-U. All the CeO<sub>2</sub>-containing catalysts exhibited positive soot conversion trends for an increasing reaction temperature, and soot combustion was completed at about 650 °C for the less reactive materials (Ce-SCS and Ce-M catalysts).

**Table 4**  
Soot oxidation activity results, under “loose” and “tight” contact conditions of the prepared CeO<sub>2</sub>-based materials.

Catalyst	Contact	T <sub>10%</sub> (°C)	T <sub>50%</sub> (°C)	T <sub>90%</sub> (°C)	T <sub>100%</sub> (°C)
Ce-NC	Loose contact	417	477	584	622
	Tight contact	396	400	425	618
Ce-NR	Loose contact	429	536	623	656
	Tight contact	381	416	455	625
Ce-NC/ZSM-5	Loose contact	394	525	590	620
	Tight contact	335	439	481	567
Ce-M	Loose contact	398	538	604	630
	Tight contact	374	464	510	590
Ce-SCS	Loose contact	436	580	633	670
	Tight contact	392	476	558	638
Printex-U	–	540	620	665	695

Different conversions have been observed: better results, in terms of T<sub>50%</sub> and T<sub>90%</sub> values (temperatures necessary to attain 50 and 90% soot conversion, respectively), have been reached for both Ce-NC and Ce-NC/ZSM-5 compared to the Ce-NR, Ce-M and Ce-SCS catalysts (values in Table 4). In other words, Ce-NC appears to be the most promising catalyst and showed that small CeO<sub>2</sub>-truncated nanocubes are highly active in soot oxidation, most likely due to the abundance of coordinative unsaturated atomic sites in the (1 0 0) and (1 1 0) exposed surfaces [43,62–65]. Moreover, the relative number of low coordination surface sites (e.g. edge and corner atoms) increases with decreasing particle size [63,64]. On the other hand, lower catalytic activity has been obtained for Ce-SCS, although the reducibility of the surface CeO<sub>2</sub>, as revealed by H<sub>2</sub>-TPR analysis, is easier (vide supra).

Likewise, Ce-NC/ZSM-5 exhibited a better performance, in terms of T<sub>peak</sub> (temperature necessary to reach 100% soot conversion), than all the other nanoshaped CeO<sub>2</sub>-materials, even though the amount of the active phase (50 wt.% CeO<sub>2</sub> on the surface of ZSM-5) is lower. As expected, a higher relative amount of Ce-NC improved the overall activity of the Ce-NC/ZSM-5 catalyst, due to the larger number of reactive (1 0 0) and (1 1 0) surfaces. However, the results have not been reported for the sake of brevity.

The shape of soot conversion curves for Ce-NC, Ce-NC/ZSM-5 and Ce-NR catalysts strongly depends on the crystalline planes and thus on the exposed surfaces. In fact, the CO<sub>x</sub> formation (mainly CO<sub>2</sub>) as a function of temperature (Fig. 9A and B) has a multimodal distribution, thus indicating the presence of different reactive surfaces. On the other hand, unimodal distributions (one peak or “mode”) can be observed for both Ce-M and Ce-SCS materials, and hence sigmoidal soot conversion trends may appear with the latter.

These results suggest the surface-sensitivity [66–68] of soot oxidation over the prepared catalysts when the reaction temperature is above ca. 410 °C. The cause of this structure sensitivity can be ascribed either to the fact that low coordination surface sites exhibit higher reactivity, because of the low energy charge fluctuations in their d-bands [64,69] or due to the quantum size effects that are produced when electrons are confined within a small volume [64,70].

Better results (e.g. in terms of the onset of soot oxidation, T<sub>10%</sub>) have been obtained at lower temperatures for high surface area materials, thus reflecting the key role of the surface area on catalytic activity. The surface-insensitivity observed at low temperatures can be attributed to the presence of adsorbed species (e.g. hydroxyl groups, inert molecules, etc.) on the solid surface, which weaken the reactant–catalyst surface interactions or are inactive in the oxidation reaction, in both cases masking the catalyst surface [68]. During the catalytic reaction, both the reactants and products can remain for a certain period of time on the catalyst surface and block the active sites. Moreover, their presence can influence the electronic structure of the substrate and thus the reactivity of the catalyst [71].



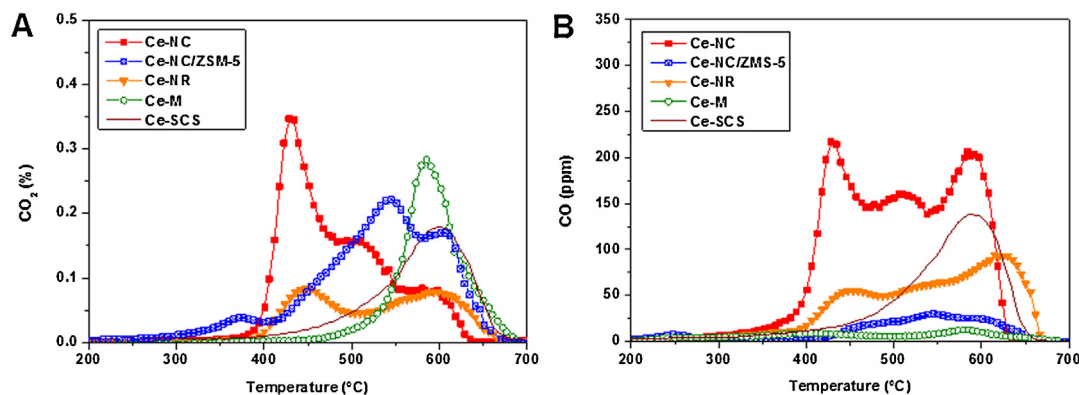


Fig. 9. (A)  $\text{CO}_2$  concentration (%) and (B) CO concentration (ppm) obtained in “loose” contact conditions.

In order to analyze the stability of the most promising catalyst, three successive catalytic cycles have been performed for soot oxidation on the Ce-NC/ZSM-5. Fig. 10 shows the performances of the Ce-NC/ZSM-5 catalyst, as a function of temperature, on each heating run and then kept at 750 °C for 1 h. As a whole, comparable performances have been achieved during three catalytic cycles and no significant deactivation was observed in terms of total soot conversion. A slight reduction of soot conversion at low temperature is likely due to a lower amount of surface-adsorbed oxygen species (i.e.  $\text{O}_2^{2-}$ ,  $\text{O}^-$ ,  $\text{OH}^-$ ,  $\text{CO}_3^{2-}$ ), which play a key role in oxidation catalysis (via spillover phenomena or “remote control effect”) [72–75].

Similar catalytic behaviour can be observed under “tight” contact conditions (Fig. 11). In the present case, an improvement in the catalytic activities (namely  $T_{10\%}$ ,  $T_{50\%}$ ,  $T_{90\%}$  and  $T_{\text{peak}}$ ) has been obtained for all the prepared catalysts, with respect to loose-conditions (values in Table 4), due to the stronger soot–catalyst interactions and to the more effective mass transport phenomena. The soot conversion curves rapidly increase for all the catalysts, as a function of temperature, since diffusive phenomena are limited under “tight” conditions. However, the conversion curves of the Ce-M and Ce-SCS samples exhibit a lower slope indicating that mass transport limitations (e.g. Knudsen diffusion) occur in the mesoporous framework. The conversion values reached above 370 °C confirm the surface-sensitivity of soot combustion, whereas the reaction behaves as structure insensitive at lower temperatures. Interestingly, the Ce-NC/ZSM-5 showed comparable performances during three successive catalytic cycles (Fig. 12), thus suggesting the good stability of this multicomponent catalyst

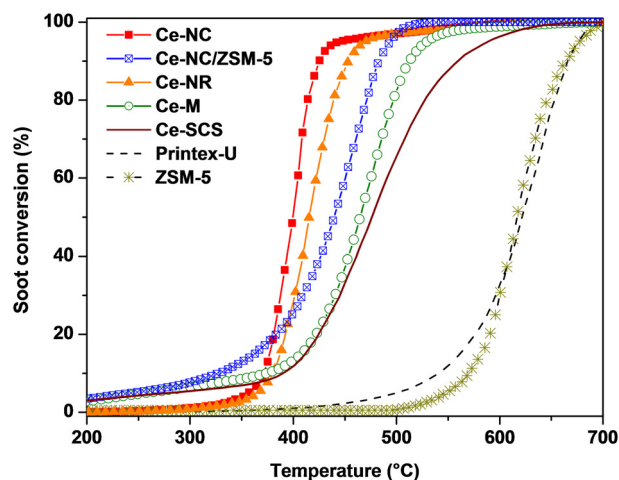


Fig. 11. Soot conversion, as a function of temperature, over  $\text{CeO}_2$ -based catalysts, pure ZSM-5 and Printex-U (no catalyst) using “tight” contact conditions.

in tight conditions. Similar results have been obtained with the Ce-NR sample (not reported for the sake of brevity).

As a consequence, the soot oxidation over the ceria catalysts could be classified as a reaction that displays both surface-sensitive and surface-insensitive behaviour, depending on the experimental conditions.

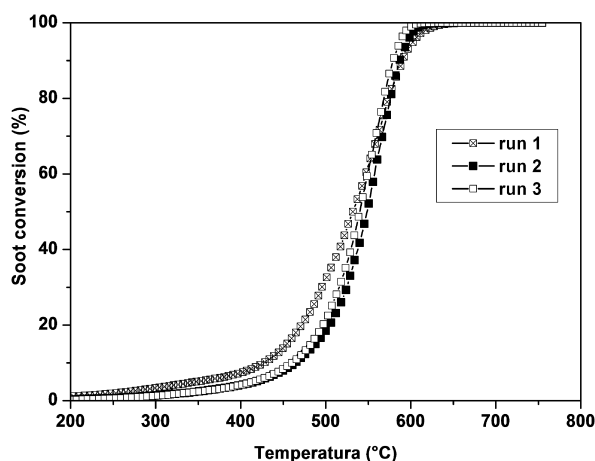


Fig. 10. Stability study of the Ce-NC/ZSM-5 catalyst for three successive catalytic cycles (“loose” contact conditions).

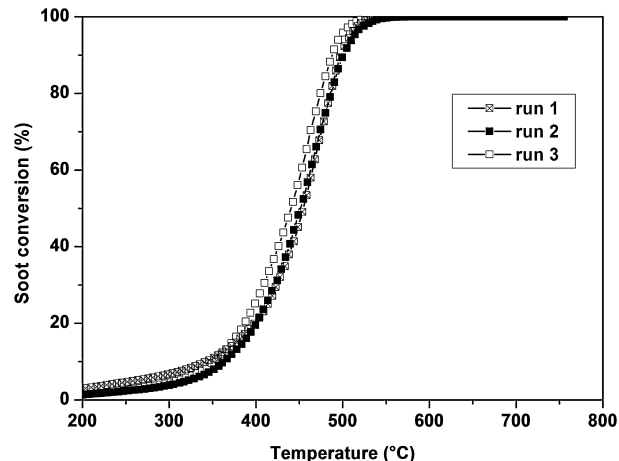


Fig. 12. Stability study of the Ce-NC/ZSM-5 catalyst for three successive catalytic cycles (“tight” contact conditions).

## 4. Conclusions

A set of ceria-based nanomaterials, with different topological and textural properties (Ce-NC, Ce-NR, Ce-NC/ZSM-5, Ce-M and Ce-SCS) has been synthesized to study the shape-dependency activity of CeO<sub>2</sub> towards soot combustion under different experimental conditions (namely in “loose” and “tight” contact). As a result, the best performances, in terms of the total oxidation of soot, have been achieved for the Ce-NC sample, likely due to the abundance of coordinative unsaturated atomic sites in the (1 0 0) and (1 1 0) exposed surfaces of the CeO<sub>2</sub> truncated nanocubes. However, better results, in terms of the onset of soot oxidation, have been obtained for the high-surface-area materials (Ce-M, Ce-NC/ZSM-5 and Ce-SCS), thus showing the main role played by the surface area at low temperatures. Activity tests have shown the surface-sensitivity of soot oxidation over the prepared materials when the reaction temperature is above either 410 °C or 370 °C (in “loose” or “tight” conditions, respectively). Conversely, the reaction seems surface insensitive at lower temperatures since the presence of adsorbed species partially “masks” the catalyst surface. In other words, soot oxidation over ceria compounds could be considered as a reaction that displays both surface-sensitive and surface-insensitive behaviour, depending on the operating conditions. However, it must be pointed out that these results are related to specific experimental conditions, and hence they cannot be representative (at all) of realistic diesel exhaust conditions.

## Acknowledgment

The Ministero dell'Università e della Ricerca (MIUR) (grant number: RBFR12LS6M.001) is acknowledged for sponsoring this research activity (FIRB – Futuro in Ricerca 2012).

## References

- [1] A. Trovarelli, P. Fornasiero, *Catalysis by Ceria and related Materials*, 2nd ed., Imperial College Press, London, 2013, pp. 565–621.
- [2] R.M. Heck, R.J. Farrauto, S.T. Gulati, *Catalytic Air Pollution Control: Commercial Technology*, 3rd ed., Wiley-VCH, Hoboken, NJ, 2006, pp. 1–518.
- [3] G. Ertl, H. Knözinger, F. Schüth, J. Weitkamp, *Handbook of Heterogeneous Catalysis*, 2nd ed., Wiley-VCH, Weinheim, 2008, pp. 2274–2344.
- [4] A. Bueno-López, *Appl. Catal. B* 146 (2014) 1–11.
- [5] R. Burch, *Catal. Rev.* 46 (2004) 271–333.
- [6] A. Russell, W.S. Epling, *Catal. Rev. Sci. Eng.* 53 (2011) 337–423.
- [7] P. Eastwood, *Critical Topics in Exhaust Gas Aftertreatment*, Research Studies Press Ltd., Baldock, England, 2000, pp. 400.
- [8] S. Bensaid, J.C. Caroca, N. Russo, D. Fino, *Can. J. Chem. Eng.* 89 (2011) 401–407.
- [9] E. Aneggi, D. Wiaters, C. de Leitenburg, J. Llorca, A. Trovarelli, *ACS Catal.* 4 (2014) 172–181.
- [10] I. Atribak, F.E. Lopez-Suarez, A. Bueno-Lopez, A. Garcia-Garcia, *Catal. Today* 176 (2011) 404–408.
- [11] M. Issa, C. Petit, A. Brillard, J.-F. Brilhac, *Fuel* 87 (2008) 740–750.
- [12] E. Aneggi, C. de Leitenburg, A. Trovarelli, *Catal. Today* 181 (2012) 108–115.
- [13] S. Bensaid, N. Russo, D. Fino, *Catal. Today* 216 (2013) 57–63.
- [14] P.A. Kumar, M.D. Tanwar, S. Bensaid, N. Russo, D. Fino, *Chem. Eng. J.* 207–208 (2012) 258–266.
- [15] E. Aneggi, M. Boaro, C. de Leitenburg, G. Dolcetti, A. Trovarelli, *J. Alloys Compd.* 408–412 (2006) 1096–1102.
- [16] S. Bernal, G. Blanco, J.M. Pintado, J.M. Rodríguez-Izquierdo, M.P. Yeste, *Catal. Commun.* 6 (2005) 582–585.
- [17] S. Carrettin, P. Concepción, A. Corma, J.M. López-Nieto, V.F. Puntes, *Angew. Chem., Int. Ed.* 43 (2004) 2538–2540.
- [18] Q. Fu, H. Saltsburg, M. Flytzani-Stephanopoulos, *Science* 301 (2003) 935–938.
- [19] L. Pino, A. Vita, M. Cordaro, V. Recupero, M.S. Hegde, *Appl. Catal. A* 243 (2003) 135–146.
- [20] Q. Yuan, H.H. Duan, L.L. Li, L.D. Sun, Y.W. Zhang, C.H. Yan, *J. Colloid Interface Sci.* 335 (2009) 151–167.
- [21] S. Iijima, *Nature* 354 (1991) 56–58.
- [22] S.J. Tans, A.R.M. Verschueren, C. Dekker, *Nature* 393 (1998) 49–52.
- [23] S.S. Fan, M.G. Chapline, N.R. Franklin, T.W. Tombler, A.M. Cassell, H. Dai, *Science* 283 (1999) 512–514.
- [24] A.K. Geim, K.S. Novoselov, *Nat. Mater.* 3 (2007) 183–191.
- [25] D.L. Feldheim, C.A. Foss, *Metal Nanoparticles*, Marcel Dekker, New York, 2002, pp. 1–352.
- [26] J.M. Thomas, R. Raja, *Top. Catal.* 53 (2010) 848–858.
- [27] R.A. van Santen, M. Neurock, *Molecular Heterogeneous Catalysis*, Wiley-VCH, Verlag, 2006, pp. 1–474.
- [28] G.A. Somorjai, *Langmuir* 7 (1991) 3176–3182.
- [29] G.A. Somorjai, J.Y. Park, *Catal. Lett.* 115 (2007) 87–98.
- [30] S. Chowdhury, K.-S. Lin, *J. Nanomater.* 2011 (2011) 1–16.
- [31] W.Q. Han, W. Wen, J.C. Hanson, X.W. Teng, N. Marinkovic, J.A. Rodriguez, *J. Phys. Chem. C* 113 (2009) 21949–21955.
- [32] N. Ta, J. Liu, S. Chenna, P.A. Crozier, Y. Li, A. Chen, W.J. Shen, *J. Am. Chem. Soc.* 134 (2012) 20585–20588.
- [33] C.S. Pan, D.S. Zhang, L.Y. Shi, J.H. Fang, *Eur. J. Inorg. Chem.* 15 (2008) 2429–2436.
- [34] Z.L. Wu, M.J. Li, S.H. Overbury, *J. Catal.* 285 (2012) 61–73.
- [35] N.K. Renuka, A.K. Praveen, C.U. Aniz, *Micropor. Mesopor. Mater.* 169 (2013) 35–41.
- [36] X. Du, D. Zhang, L. Shi, R. Gao, J. Zhang, *J. Phys. Chem. C* 116 (2012) 10009–10016.
- [37] W.I. Hsiao, Y.S. Lin, Y.C. Chen, C.S. Lee, *Chem. Phys. Lett.* 441 (2007) 294–299.
- [38] K.B. Zhou, X. Wang, X.M. Sun, Q. Peng, Y.D. Li, *J. Catal.* 229 (2005) 206–212.
- [39] Z.X. Yang, T.K. Woo, M. Baudin, K. Hermansson, *J. Chem. Phys.* 120 (2004) 7741–7749.
- [40] T.X.T. Sayle, M. Cantoni, U.M. Bhatta, S.C. Parker, S.R. Hall, G. Mobus, M. Molinari, D. Reid, S. Seal, D.C. Sayle, *Chem. Mater.* 24 (2012) 1811–1821.
- [41] M. Nolan, S. Grigoleit, D.C. Sayle, S.C. Parker, G.W. Watson, *Surf. Sci.* 576 (2005) 217–229.
- [42] H.-X. Mai, L.-D. Sun, Y.-W. Zhang, R. Si, W. Feng, H.-P. Zhang, H.-C. Liu, C.-H. Yan, *J. Phys. Chem. B* 109 (2005) 24380–24385.
- [43] S. Agarwal, L. Lefferts, B.L. Mojet, *ChemCatChem* 5 (2013) 479–489.
- [44] P. Ji, J. Zhang, F. Chen, M. Anpo, *J. Phys. Chem. C* 112 (2008) 17809–17813.
- [45] A. Civera, M. Pavese, G. Saracco, V. Specchia, *Catal. Today* 83 (2003) 199–211.
- [46] J.P.A. Neeft, M. Makkee, J.A. Moulijn, *Appl. Catal. B* 8 (1996) 57–78.
- [47] S.O. Baek, R.A. Field, M.E. Goldstone, P.W. Kirk, J.N. Lester, R.A. Perry Water, *Air Soil Pollut.* 60 (1991) 279–300.
- [48] S.C. Laha, R. Ryoo, *Chem. Commun.* (2003) 2138–2139.
- [49] B. Puertolas, B. Solsona, S. Agouram, R. Murillo, A.M. Mastral, A. Aranda, S.H. Taylor, T. Garcia, *Appl. Catal. B* 93 (2010) 395–405.
- [50] M. Hussain, N. Russo, G. Saracco, *Chem. Eng. J.* 166 (2011) 138–149.
- [51] G. Wulff, *Z. Kristallogr. Mineral.* 34 (1901) 449–530.
- [52] A.S. Barnard, *J. Phys. Chem. B* 110 (2006) 24498–24504.
- [53] M. Machida, Y. Murata, K. Kishikawa, D. Zhang, K. Ikeue, *Chem. Mater.* 20 (2008) 4489–4494.
- [54] S. Agarwal, L. Lefferts, B.L. Mojet, D.A.J.M. Ligthart, E.J.M. Hensen, D.R.G. Mitchell, W.J. Erasmus, B.G. Anderson, E.J. Olivier, J.H. Neethling, A.K. Datye, *ChemSusChem* 6 (2013) 1898–1906.
- [55] F. Giordano, A. Trovarelli, C. de Leitenburg, M. Giona, *J. Catal.* 193 (2000) 273–282.
- [56] G. Ranga Rao, *Bull. Mater. Sci.* 22 (1999) 89–94.
- [57] G. Ranga Rao, J. Kašpar, S. Meriani, R.D. Monte, M. Graziani, *Catal. Lett.* 24 (1994) 107–112.
- [58] P. Fornasiero, R. Di Monte, G. Ranga Rao, J. Kašpar, S. Meriani, A. Trovarelli, M. Graziani, *J. Catal.* 151 (1995) 168–177.
- [59] G. Ranga Rao, B.G. Mishra, *Bull. Catal. Soc. Ind.* 2 (2003) 122–134.
- [60] G. Zhang, Z. Shen, M. Liu, C. Guo, P. Sun, Z. Yuan, B. Li, D. Ding, T. Chen, *J. Phys. Chem. B* 110 (2006) 25782–25790.
- [61] B.M. Reddy, A. Khan, Y. Yamada, T. Kobayashi, S. Lorient, J.-C. Volta, *J. Phys. Chem. B* 107 (2003) 5162–5167.
- [62] W.C. Conner, J.L. Falconer, *Chem. Rev.* 95 (1995) 759–788.
- [63] R.A. Van Santen, *Acc. Chem. Res.* 42 (2009) 57–66.
- [64] N. Musselwhite, G.A. Somorjai, *Top. Catal.* 56 (2013) 1277–1283.
- [65] Z. Quan, Y. Wang, J. Fang, *Acc. Chem. Res.* 46 (2013) 191–202.
- [66] M. Boudart, *Adv. Catal.* 20 (1969) 153–177.
- [67] G. Somorjai, *Catal. Lett.* 7 (1990) 169–182.
- [68] G.A. Somorjai, *J. Carrazza, Ind. Eng. Chem. Fundam.* 25 (1986) 63–69.
- [69] L. Falicov, G.A. Somorjai, *Proc. Nat. Acad. Sci. U.S.A.* 82 (1985) 2207–2211.
- [70] M. Valden, X. Lai, D.W. Goodman, *Science* 281 (1998) 1647–1650.
- [71] B. Hammer, *Phys. Rev.* 63 (2001) 2054231–2054238.
- [72] D. Carson, G. Coudurier, J.C. Védrine, A. Laarif, F. Theobald, *J. Chem. Soc. Faraday Trans. I* 79 (1983) 1921–1929.
- [73] J.M.M. Millet, H. Ponceblanc, G. Coudurier, J.M. Herrmann, J.C. Védrine, *J. Catal.* 142 (1993) 381–391.
- [74] L.T. Weng, B. Delmon, *Appl. Catal. A: Gen.* 81 (1992) 141–213.
- [75] J.C. Védrine, *Appl. Catal. A: Gen.* 474 (2014) 40–50.